

# New lightning-derived vertical total electron content data provides unique global ionospheric measurements

Erin H Lay<sup>1</sup>, Jeffery Tippmann<sup>2</sup>, Kyle Wiens<sup>2</sup>, Sarah E McDonald<sup>3</sup>, Anthony James Mannucci<sup>4</sup>, Xiaoqing Pi<sup>4</sup>, Anthea J. Coster<sup>5</sup>, Richard Marc Kippen<sup>1</sup>, and Robert Joseph Redmon<sup>6</sup>

<sup>1</sup>Los Alamos National Laboratory (DOE)

<sup>2</sup>Los Alamos National Laboratory

<sup>3</sup>Naval Research Laboratory

<sup>4</sup>Jet Propulsion Laboratory, California Institute of Technology

<sup>5</sup>Haystack Observatory Mass. Inst. Technology

<sup>6</sup>National Oceanic and Atmospheric Administration (NOAA)

November 23, 2022

## Abstract

A newly-released, novel ionospheric dataset of global gridded vertical total electron content (VTEC) is introduced in this paper. This VTEC dataset, provided by Los Alamos National Laboratory (LANL), is derived from very-high frequency (VHF; defined as 30-300 MHz) broadband radio-frequency (RF) measurements of lightning made by U.S. Department of Defense sensing systems on board Global Positioning System (GPS) satellites. This paper presents the new dataset (LANL VTEC), discusses the errors inherent in VHF TEC estimation due to ionospheric dispersion, and compares the LANL VTEC to two community standard VTEC gridded products: Jet Propulsion Laboratory's Global Ionospheric Model (JPL GIM) and the CEDAR community's Open Madrigal VTEC gridded measurements of L-band GNSS (global navigation satellite systems) TEC. We find that the LANL VTEC data has an offset of 3 TECU from CEDAR Madrigal GNSS VTEC, and a full-width-half-maximum (FWHM) of 6 TECU. In comparison, the offset between LANL VTEC and the JPL GIM model is -3 TECU, but with a FWHM of 5 TECU. We also compare to Jason-3 VTEC measurements over the ocean, finding an offset of less than 0.5 TECU and a FWHM of < 5 TECU. Because this technique uses a completely different methodology to determine TEC, the sources of errors are distinct from the typical ground-based GNSS L-band (GHz) TEC measurements. Also, because it is derived from RF lightning signals, this dataset provides measurements in regions that are not well covered by ground-based GPS measurements, such as over oceans and over central Africa.

1 **New lightning-derived vertical total electron content data provides unique global**  
2 **ionospheric measurements.**

3 **Erin H. Lay<sup>1</sup>, Jeffery D. Tippmann<sup>1</sup>, Kyle C. Wiens<sup>1</sup>, Sarah E. McDonald<sup>2</sup>, Anthony J.**  
4 **Mannucci<sup>3</sup>, Xiaoqing Pi<sup>3</sup>, Anthea Coster<sup>4</sup>, R. Marc Kippen<sup>1</sup>, and Rob Redmon<sup>5</sup>**

5 <sup>1</sup> Los Alamos National Laboratory, Los Alamos, NM 87545.

6 <sup>2</sup> Space Science Division, Naval Research Laboratory, Washington, DC.

7 <sup>3</sup> Jet Propulsion Laboratory, California Institute of Technology, Pasadena, CA 91109.

8 <sup>4</sup> MIT Haystack Observatory, Westford, MA, 01886.

9 <sup>5</sup> National Centers for Environmental Information, NOAA, Boulder, CO, USA.

10

11 Corresponding author: Erin Lay (elay@lanl.gov)

12 **Key Points:**

- 13 • New global gridded VTEC dataset derived from RF measurements from lightning  
14 emissions during entire year of 2018 has been released.
- 15 • VTEC product adds new global coverage in areas with few GNSS receivers (ocean and  
16 continental Africa).
- 17 • The VTEC values, generated from VHF RF data, show bias in Madrigal dataset and  
18 differences to JPL-GIM model derived VTEC.

19

**20 Abstract**

21 A newly-released, novel ionospheric dataset of global gridded vertical total electron content  
22 (VTEC) is introduced in this paper. This VTEC dataset, provided by Los Alamos National  
23 Laboratory (LANL), is derived from very-high frequency (VHF; defined as 30-300 MHz)  
24 broadband radio-frequency (RF) measurements of lightning made by U.S. Department of  
25 Defense sensing systems on board Global Positioning System (GPS) satellites. This paper  
26 presents the new dataset (LANL VTEC), discusses the errors inherent in VHF TEC estimation  
27 due to ionospheric dispersion, and compares the LANL VTEC to two community standard  
28 VTEC gridded products: Jet Propulsion Laboratory's Global Ionospheric Model (JPL GIM) and  
29 the CEDAR community's Open Madrigal VTEC gridded measurements of L-band GNSS (global  
30 navigation satellite systems) TEC. We find that the LANL VTEC data has an offset of 3 TECU  
31 from CEDAR Madrigal GNSS VTEC, and a full-width-half-maximum (FWHM) of 6 TECU. In  
32 comparison, the offset between LANL VTEC and the JPL GIM model is -3 TECU, but with a  
33 FWHM of 5 TECU. We also compare to Jason-3 VTEC measurements over the ocean, finding  
34 an offset of less than 0.5 TECU and a FWHM of  $< 5$  TECU. Because this technique uses a  
35 completely different methodology to determine TEC, the sources of errors are distinct from the  
36 typical ground-based GNSS L-band (GHz) TEC measurements. Also, because it is derived from  
37 RF lightning signals, this dataset provides measurements in regions that are not well covered by  
38 ground-based GPS measurements, such as over oceans and over central Africa.

39

40 **Plain Language Abstract**

41 The ionosphere is a region of the atmosphere that is very important in communications between  
42 ground and satellite. For that reason, decades of scientific effort has been put towards developing  
43 models of the ionosphere so that we can more accurately predict what the state of the ionosphere  
44 is at any given location and time. A general product produced by many of these models is the  
45 vertical total electron content (VTEC), which is the vertically-integrated electron density at a  
46 particular location at a particular time. The majority of these models use measurements of TEC  
47 from ground-based receivers or instruments, meaning that abundant measurements that go into  
48 the models often lack data from over the oceans, or in technologically-limited regions of the  
49 world (e.g. Africa). Here we present a new VTEC dataset that is derived from lightning strokes  
50 detected with U.S. Department of Defense sensing systems on GPS satellites. Because the data  
51 set uses naturally-occurring lightning for its source, it does not have the same limitations as  
52 ground-based TEC measurements, and can provide an additional source of validation data for  
53 ionospheric models. We introduce the data set and compare it with community-accepted VTEC  
54 models and measurement.

55

## 56 **1 Introduction**

57         The ionosphere is a layer of plasma in the Earth's atmosphere (from 60 to more than  
58 2000 km altitude) (Kelley 2009). The nature of this plasma impacts natural and man-made  
59 electromagnetic signals that interact with it. This interaction occurs in many forms, such as  
60 refraction, absorption, dispersion and scintillation. Being able to nowcast and forecast the  
61 ionospheric state and variability on a global scale is important for understanding associated  
62 communication impacts. Variability in the ionosphere is driven by several external sources,  
63 roughly ordered as follows from the most globally to regionally significant: solar forcing solar  
64 EUV flux (photoionization), solar flares, and geomagnetic storms (e.g. Shunk and Sojka, 1996;  
65 Mannucci et al., 2005; Yizengaw et al., 2006; Coster and Skone, 2008; Wang et al., 2010); and  
66 lower atmosphere forcing gravity waves, thunderstorms, earthquakes, and explosions (e.g. Lay  
67 2018; Azeem et al., 2015; Lay et al., 2015; Galvan et al., 2011).

68         Empirical and physics-driven models have been developed to accurately analyze and  
69 forecast the state of the ionosphere (e.g. Mannucci et al., 1998; Mandrake et al., 2005, Scherliess  
70 et al., 2006; Nava et al., 2008, Scherliess et al., 2009; Bilitza et al., 2011). These models are built  
71 on decades of ionospheric observations. However, the ionosphere is extremely difficult to  
72 accurately measure continuously on a global scale, and therefore it is difficult to detect and  
73 predict variations due to individual events from the climatological average. Ground-based Global  
74 Navigation Satellite System (GNSS) total electron content (TEC) measurements are a widely-  
75 used global data source for use in ionospheric modeling based on their geographic ubiquity and  
76 nearly continuous operation. However, with current ground based capabilities, these  
77 measurements are sparse or unavailable over oceans and some regions of the world such as  
78 central Africa.

79 GNSS receivers calculate the integrated electron density along a line of sight from  
80 satellite to receiver (slant TEC) by measuring the dispersive contributions to two separate GHz-  
81 frequency satellite signals. TEC is then determined by combining the less precise but absolute  
82 pseudorange measurement with the precise but ambiguous phase differential measurement.  
83 Inherent timing uncertainties in the GHz frequency bands limits the accuracy of the absolute  
84 TEC derived from this method to 2-5 TECU, where  $1 \text{ TECU} = 1 \times 10^{16} \text{ electrons/m}^2$  (Burrell et.  
85 al, 2009). Slant TEC measurements are often converted to vertical TEC (VTEC) values by using  
86 a geometrical mapping function based on the satellite elevation angle and an assumed  
87 ionospheric height (Burrell et al., 2009; Mannucci et al., 1998), typically between 350 and 400  
88 km.

89 We present a novel dataset that provides an independent comparison of the much-utilized  
90 GNSS TEC measurements and, in addition provides TEC measurements in low-coverage areas  
91 (oceans, economically disadvantaged areas). The new data is derived from unique measurements  
92 of lightning events, each of which produces a broadband radio signal that gets dispersed through  
93 the ionosphere before it is detected on satellite receivers (Jacobson et al., 1999; Roussel-Dupre et  
94 al., 2001). Each measured lightning provides a snapshot of the ionospheric conditions at that  
95 instant, and many lightning measurements over time and around the globe provide unique  
96 measurements for ionospheric science. With 93% of the LANL VTEC measurements covered by  
97 existing GPS ground stations, these matching measurements can be used for improving  
98 calibration of the GPS TEC measurements in space weather models. The remaining 7% of the  
99 LANL VTEC measurements that add new coverage, while small in quantity due to the non-  
100 continuous nature of the source events, can still be used to fill the gaps in models to improve the  
101 global scale TEC outputs in these regions during those time periods.

102 In this paper, we introduce the new Los Alamos National Laboratory vertical total  
 103 electron content (LANL VTEC) product. We then compare the LANL VTEC data with GPS-  
 104 measured VTEC from the CEDAR Madrigal GNSS VTEC product (Rideout and Coster, 2006;  
 105 Vierinen et al., 2016), JPL GIM VTEC (Mannucci et al., 1998; Iijima et al., 1999), and Jason-3  
 106 VTEC measurements derived from ocean altimetry satellites.

## 107 **2 Datasets**

### 108 **2.1 LANL VTEC Data**

109 Los Alamos National Laboratory (LANL) vertical TEC measurements are derived from  
 110 U.S. Department of Defense broadband radio-frequency (RF) sensing systems on Global  
 111 Positioning System (GPS) satellites that measure transient events in the very-high frequency  
 112 (VHF, defined as 30-300 MHz) range. Detection of an event by multiple satellites allows  
 113 determination of the event location, based on minimization of the time of arrival at each satellite.  
 114 As RF signals from transient broadband lightning events travel through the ionosphere, they are  
 115 dispersed, so lower frequencies arrive later in time than higher frequencies (Lay et al., 2011;  
 116 Moses and Jacobson, 2004; Jacobson et al., 1999). This dispersion can be used to determine the  
 117 slant total electron content (STEC, or the integrated electron density along the line of sight  
 118 between each lightning location and the GPS satellite in medium Earth orbit (MEO)). To  
 119 determine the STEC from a recorded lightning signal, we fit the time delay versus frequency  
 120 spectrogram to the first order approximation of the Appleton-Hartree Equation (Lay et al., 2011;  
 121 Eqn. 6, and Eqn. 7a):

$$122 \quad n^2 = 1 - \frac{X(1-X)}{(1-X) - \frac{1}{2Y_T^2} + s \sqrt{\frac{1}{4Y_T^4} + (1-X)^2 Y_T^2}}; \quad (\text{Eqn. 1})$$

123 where  $X = f_p^2 / f^2$ ;  $Y = f_{ce} / f$ ;  $Y_L = Y \cos \theta$ ;  $Y_T = Y \sin \theta$ ;  $f_p$  is the plasma frequency of the  
 124 ionosphere,  $f$  is the wave radio frequency,  $f_{ce}$  is the electron cyclotron frequency and  $\theta$  is the  
 125 angle between the propagation and the magnetic field vectors. The variable  $s = \pm 1$ , represents  
 126 the fast and slow modes in the plasma. When  $X$  and  $Y$  are small compared with unity, this  
 127 relation can be estimated by a Taylor expansion, taken to first order,  $n \approx 1 - \frac{1}{2} \frac{f_p^2}{f^2} + \dots$ . This  
 128 approximation gives a first order time delay of

$$129 \quad \tau(f) = \frac{R}{c} + \frac{C_1}{f^2} + \dots \quad (\text{Eqn. 2})$$

130 where  $R$  is the source-to-sensor distance,  $c$  is the speed of light, and  $C_1 = e^2 /$   
 131  $8\pi^2 c \epsilon_0 m_e \int_0^L N_e(l) dl$ . The integral of electron density,  $N_e$ , in this term is taken along the line-  
 132 of-sight path between the source and sensor, and thus represents the line-of-sight STEC (Lay et  
 133 al., 2011). LANL VTEC is derived from individual STEC measurements determined by using  
 134 the first-order approximation to the A-H Equation (Eqn. 2), and implementing a broadband  
 135 fitting routine similar to that described in Lay et al., 2011. Each lightning stroke can produce  
 136 several measurements of STEC along the various lines-of-sight to all satellites detecting it.

137 A mapping factor of  $VTEC = STEC \sqrt{1 - \left[ \cos(el) / \left(1 + \frac{H}{R_e}\right) \right]^2}$  (Burrell et al., 2009;  
 138 Jakowski et al., 2011), then is used to project the STEC to a vertical TEC (VTEC), where  $el$  is  
 139 the elevation angle of the satellite with respect to the lightning location,  $H$  is chosen to be 350  
 140 km, the assumed height of the ionospheric pierce point (IPP) (though altitudes between 350 to  
 141 450 have been used by different groups depending on specific model approach), and  $R_e$  is the  
 142 radius of the Earth. VTEC measurements from individual lightning events are combined in  $5^\circ$   
 143 latitude  $\times$   $5^\circ$  longitude geographical bins and 1-hour time bins. Latitude bins are limited to

144 between  $-60^\circ$  and  $60^\circ$ , since very few lightning strokes occur outside those limits. The median  
145 VTEC in a given bin is provided in the LANL VTEC product. This binning creates a sparse  
146 global VTEC product from lightning events. An example time period is shown in Figure 1  
147 (bottom panel). The currently released data includes all of 2018, globally. There are 143,541 grid  
148 cells with LANL VTEC measurements over this time period. The comparisons in this paper of  
149 LANL VTEC to Madrigal VTEC and JPL GIM VTEC are on this entire data set.

150

## 151 **2.2 Estimated Error on LANL VTEC**

152 While the same first order approximation is made in order to determine GNSS TEC and  
153 VHF TEC, the error introduced by the approximation is larger at lower frequencies due to  
154 decreased fidelity of the  $X \ll 1$  and  $Y \ll 1$  assumptions. Also, the signal refracts much more  
155 significantly at lower frequencies, meaning that the line-of-sight approximation is less valid as  
156 well (Lay et al., 2011; Roussel-Dupre et al., 1999). Previous studies show that STEC error can be  
157 larger than 10 TECU for frequencies lower than 45 MHz, but the effect is mitigated when using a  
158 broadband signal to fit time-delay versus frequency for many frequencies at once. Because the  
159 assumptions on  $X$  and  $Y$  are valid in the GHz regime (GNSS TEC), the majority of the error on  
160 GNSS slant TEC estimation comes from uncertainty in resolving the absolute time delay in the  
161 GPS signal due to hardware limitations (Sardón and Zarraoa, 1997), rather than uncertainty due  
162 to dispersion and ray bending effects.

163 In this work, we estimate the ionospheric-induced error on LANL VTEC based on a  
164 realistic sampling of lightning events around the world. We use a similar ray-tracing technique to  
165 that of Lay et al., 2011, but with realistic ionospheric electron density profiles from the

166 NeQuick2 model (Nava et al., 2008) for the specific day and location of the simulation. The  
167 locations and times of the simulated lightning signals are generated from a random sample of  
168 lightning locations detected by the World Wide Lightning Location Network (WWLLN)  
169 (Dowden et al., 2002; Lay et al., 2004; Abarca et al., 2010) during two days in 2014: 14 January  
170 and 14 July. The year 2014 was chosen due to high solar activity at that time, and, thus, high  
171 electron density levels to bound the error on the high end of the TEC distribution. Most years  
172 will have lower overall VTEC values, leading to lower VTEC errors.

173       To estimate a realistic error distribution, we created an electron density altitude profile  
174 along lines of sight for the chosen random sample of WWLLN lightning events (location and  
175 time) to all GPS satellites within view. Along these lines of sight, we used the NeQuick2 model  
176 (Nava et al., 2008) with 1-km vertical spacing to provide the profile shape, including the height  
177 of the peak electron density (hmF2). The NeQuick2 model was chosen for its fast execution  
178 time, ease of use via command line interface, and ease of modeling the electron profile along the  
179 line of sight, as opposed to vertically. We then used the Utah State University Global  
180 Assimilation of Ionospheric Measurements (USU GAIM) model (Schunk et al., 2004; Decker  
181 and McNamara, 2007) to scale the overall profile as follows. An estimate of the STEC along the  
182 simulated line-of-sight was made by projecting vertical TEC USU GAIM onto each line of sight  
183 given above. We then scale the profile to give the calculated USU GAIM STEC along the line of  
184 sight. This mapping, as opposed to integrating USU GAIM along the line of sight, was also  
185 chosen for computational speed. Our goal was to model a realistic profile in terms of shape, peak  
186 electron density altitude (hmF2), and peak electron density (nmF2) at the time and location.

187       These STECs and electron density profiles form the “truth” ionosphere that we use to  
188 compare with the estimated ray-traced TEC along each line of sight. The collection of lightning-

189 to-sensor paths used in the simulation represent a realistic configuration of possible on-orbit  
190 measurements of lightning, with as realistic ionospheric conditions as possible. These paths are  
191 only used for this error simulation and representative of solar activity, and associated ionospheric  
192 variation, in the year 2014 only.

193         We use a ray tracing algorithm through this “truth” ionosphere that uses the Bouguer’s  
194 Formulation to produce a frequency-dependent time-delay using the full A-H index-of-refraction  
195 with no approximations to the dispersion relation (Born and Wolf, 1999; Lay et al., 2018). A  
196 broadband synthetic signal is produced that accounts for dispersion and ray-bending. Both modes  
197 of the Appleton-Hartree Equation are propagated and combined to produce the simulated signal  
198 arriving at a satellite through a known “truth” ionosphere. This dispersed signal is created with  
199 the highest possible fidelity to approximate a real signal arriving at a satellite. This synthetic  
200 signal is then processed through a first-order (Eqn. 2) matched filter to produce an estimate of  
201 the STEC variability due to natural ionospheric and geometric variability.

202         From this simulation, the known line-of-sight STEC determined from the “truth”  
203 ionosphere is compared with the estimated ray-traced STEC. We then convert these STEC values  
204 to VTEC based on the geometry of source-to-sensor and the mapping function above. Figure 2  
205 shows a probability density plot (counts per TECU x TECU bin / total counts) of the “truth”  
206 VTEC from the known ionosphere versus the estimated ray-traced VTEC determined as  
207 described above. This comparison gives an indication of error introduced in the LANL VTEC  
208 measurements due to ionospheric variability and geometry. Other sources of error in the  
209 uncertainty budget are not considered here. For VTEC less than about 30 TECU, where the  
210 majority of the points lie, the error introduced to LANL VTEC by ionospheric and geometric  
211 approximations is on the order of 1-2 TECU. As VTEC increases above 30 TECU, the LANL

212 VTEC gridded data begins to overestimate the true VTEC, with errors as large as 10 TECU  
213 above VTEC values of 50 TECU. These higher VTEC, and hence higher STEC, values are often  
214 correlated with lines of sight with lower elevation angles. At lower angles, the estimated STEC  
215 has inherently larger errors due to the fact that the second order approximation does not account  
216 for ray bending. The lower frequencies of VHF band bend significantly more than L-band  
217 frequencies, leading to larger errors in estimated TEC. These findings are consistent with our  
218 previous work (Lay et al., 2011). In addition, the geomagnetic mapping factor from STEC to  
219 VTEC loses fidelity at lower elevation angles.

220

### 221 **2.3 Madrigal VTEC**

222 Vertical total electron content (TEC) data, calculated from the GNSS satellite  
223 constellations, are provided through the Madrigal distributed data system  
224 (<http://www.openmadrigal.org>). Currently only the GPS and GLONASS constellations are being  
225 processed, although it is planned to include additional constellations. The algorithms used to  
226 compute the total electron content are described in Rideout and Coster (2006) and Vierinen et al.  
227 (2015). All values are then mapped to an ionospheric pierce point defined to be 350 km, and a  
228 pierce point latitude and longitude is derived. Data from approximately 6000 GNSS dual-  
229 frequency receivers world-wide are used. The data in this paper is derived from the gridded TEC  
230 product in Madrigal, where the TEC is stored in  $1^\circ \times 1^\circ$  bins at a 5-minute cadence. Each TEC  
231 value represents the median TEC of all values within the bin. An estimate of the error is also  
232 provided.

233           Because the Madrigal VTEC data (Figure 1, middle panel) is measurement-based, not all  
234 grid cells contain data, similar to the LANL VTEC data. Empty grid cells give an indication of  
235 where ground-based GPS coverage is limited globally. This gridded TEC product is available  
236 online starting in the year 2000 through the present. For comparison to LANL VTEC, we take  
237 the median of all Madrigal VTEC values contained in a given  $5^\circ \times 5^\circ \times 1$  hour bin corresponding  
238 to the LANL VTEC grid. This averaging can combine up to 300 Madrigal VTEC measurements  
239 into one measurement for comparison with LANL VTEC, with the median value being 43  
240 measurements. Nevertheless, the standard deviation of all Madrigal measurements within one  
241 LANL VTEC cell has a median value of less than 1 TECU. This indicates that this averaging  
242 technique produces a reliable estimate for comparison.

243

#### 244 **2.4 JPL GIM VTEC used in LANL VTEC comparison**

245           A technique for producing global ionospheric maps (GIM) of TEC has been developed in  
246 the 1990s (Mannucci et al., 1998; Iijima et al., 1999). It makes use of GNSS data collected from  
247 hundreds of globally distributed ground-based stations. To produce GIM, the GNSS dual-  
248 frequency pseudorange and carrier phase data are processed first to fix phase breaks and adjust  
249 the level of the precise but ambiguous phase data to the noisier but absolute range data. This  
250 phase-smoothed data, which contains much less noise than the pseudorange data alone, is then  
251 used to compute relative line-of-sight or slant TEC. The slant TEC data are modeled as vertical  
252 TEC multiplied by a geometric scaling function that depends on elevation angle, plus receiver  
253 and satellite instrumental biases. The vertical TEC is fitted to a set of 330 localized basis  
254 functions on a global grid to form a vertical TEC “surface”, which has a continuous second  
255 derivative. The satellite and receiver biases are additional parameters of the fit. The basis

256 functions are defined in a spherical sun-fixed longitude and dipole-based geomagnetic latitude  
257 reference frame that accounts for two major sources of ionospheric variability: photoionization  
258 and geomagnetic control of ionospheric dynamics. The sun-fixed frame also allows to update the  
259 different grid points with data from the same geographic longitude at different universal time,  
260 which helps to augment spatial coverage. A Kalman filter is used with the data to solve for a  
261 time series of the coefficients of the basis functions and for the satellite as well as receiver inter-  
262 frequency instrumental biases. The basis functions with the time-dependent coefficients can then  
263 be used to estimate vertical TEC globally at any location and time. The fitted biases can be  
264 removed from slant TEC measurements, and bias-removed slant TEC at any elevation angle can  
265 be reconstructed by applying the slant-to-vertical mapping function.

266         GIM is routinely produced by the Ionospheric and Atmospheric Remote Sensing (IARS)  
267 group at the Jet Propulsion Laboratory (JPL) to support NASA's Deep Space Network and space  
268 missions, solid Earth and ocean altimeter missions, and space weather research. One of the GIM  
269 products is distributed in IONEX format. The files consist of globally gridded TEC maps with  $5^\circ$   
270  $\times 5^\circ$  (geographic latitude and longitude) spatial resolutions and 2-hour cadence. The IONEX  
271 TEC map data is delivered to the NASA CDDIS data archive center (refer to the above weblink)  
272 on a daily basis. A higher-resolution version of  $2^\circ \times 2^\circ$  and 1-hour cadence is also available,  
273 which is used in this study. The IONEX maps, which are included in the Jason series altimetry  
274 data products, contain an offset of +2 TECU added to GIM in post-processing. This offset was  
275 based on early comparisons to TOPEX/Poseidon TEC in the late 1990s, which suggested that  
276 GIM maps were biased low. After years of GIM comparisons, it is not clear that GIM are biased  
277 low, but the offset for IONEX has been maintained to ensure a consistent record for altimetry,  
278 which is concerned with long-term sea level changes.

279 For this study, we use the JPL GIM or JPL VTEC term throughout this paper to represent  
280 the IONEX VTEC data of the JPL GIM at  $2^\circ \times 2^\circ$  resolutions and 1-hour cadence used in this  
281 analysis, though other GIM products are also generated at JPL. For comparison to LANL VTEC,  
282 we first interpolate onto a  $1^\circ \times 1^\circ \times 1$ -hour grid, and then take the median of JPL VTEC values  
283 contained in a given  $5^\circ \times 5^\circ \times 1$ -hour bin corresponding to the LANL VTEC grid (Figure 1, top  
284 panel). Because JPL VTEC data are already given on a time cadence of 1 hour, this averaging  
285 method only combines about 7 JPL VTEC measurements into each LANL VTEC grid cell. The  
286 standard deviation of JPL VTECs within one LANL VTEC grid cell is less than 0.5 TECU.

287

## 288 **2.5 Jason-3 VTEC**

289 Jason-3, launched in January 2016, is the most recent mission in a series of satellites  
290 (TOPEX/Poseidon, Jason-1, and Jason-2) that include dual-frequency altimeters, operating at  
291 13.575 GHz (Ku-band) and 5.3 GHz (C-band), to measure the height of the ocean surface to high  
292 accuracy. Corrections must be applied to these measurements due to the dispersive nature of the  
293 atmosphere that results in path delay of the radar signal. The ionospheric correction, or delay, is  
294 directly proportional to the electron content along the ray path and inversely proportional to the  
295 frequency ( $f$ ) squared of the signal. The difference in delay between the altimeters' dual-  
296 frequency measurements can be used to calculate the total electron content in the nadir direction  
297 (VTEC) from the spacecraft at 1354 km altitude to the surface over the oceans (Imel, 1994). TEC  
298 is calculated using the following formula:

$$299 \quad \text{Ionospheric TEC (electrons/m}^2\text{)} = -dR * f^2/40.3$$

300 where  $dR$  is the Ku-band ionospheric range correction in meters provided in the Jason-3  
301 geophysical data records (GDRs). The sampling rate of the Jason-3 instruments is 1Hz; however

302 as recommended by Imel (1994) and the Jason-3 Handbook (Dumont et al., 2017), the  
303 ionospheric range correction should be smoothed over 100 km or more to reduce instrument  
304 noise. To calculate the Jason-3 TEC used in this study, we have averaged the measurements over  
305 18 seconds, which gives us TEC with a resolution of  $\sim 2^\circ$ , or  $\sim 200$  km. The Jason-3 satellite is in  
306 an orbit with a  $66^\circ$  inclination and a 10-day repeating reference orbit, advancing approximately  
307  $2^\circ$  per day. To cover all local times takes about 90 days. While Jason-3 does not provide a dense  
308 set of measurements, it does provide a direct measure of VTEC up to an altitude of 1354 km.  
309 Altimeter data has been used extensively to validate TEC models and other measurement  
310 techniques (e.g., Mandrake et al., 2005; Yasyukevich et al., 2010). In comparing between GNSS  
311 TEC and Jason-3 TEC, it is important to account for the fact that GNSS TEC will include  
312 integrated electron density up to GNSS altitude in mid-Earth orbit (MEO: 20,200 km for GPS  
313 satellites) above the Jason-3 altitude (or plasmaspheric TEC), and thus, would be expected to be  
314 slightly higher than Jason-3 TEC by 1-2 TECU.

315

## 316 **6 Data Analysis**

317 For comparison of Madrigal VTEC and LANL, we first determine which grid cells had  
318 measurements for both data sets. The LANL VTEC contained 143,541 total cells. For the entire  
319 year of 2018 there are 134,084 joint cells between LANL VTEC and Madrigal VTEC, or 93.4%  
320 of all LANL VTEC cells are also covered by Madrigal VTEC cells. We refer to these cells as  
321 “matched” cells. Figure 3 shows a probability density of the differences (LANL VTEC –  
322 Madrigal VTEC; solid blue curve). The distribution has an offset of 2.5 TECU with a full-width,  
323 half-maximum of 6 TECU. Figure 4a shows a probability density plot of Madrigal VTEC (x-  
324 axis) versus LANL VTEC (y-axis) for all matched grid cells. Again, the slight offset of about 2.5

325 TECU for LANL VTEC is evident compared to Madrigal VTEC, but the distribution clusters  
326 well around a line of slope = 1 for the majority of TEC values. The LANL VTEC higher estimate  
327 for VTEC values is also evident in this figure, as well as the LANL VTEC tendency to produce  
328 larger overestimates at higher VTEC, as shown in Figure 2.

329         We then do the same comparison of joint grid cells between JPL GIM VTEC and LANL  
330 VTEC. Because JPL GIM is a global model it can be compared with LANL VTEC both where  
331 Madrigal VTEC data is existing (143,541 cells) and where LANL VTEC adds new coverage  
332 compared with GNSS measurements (9,457 cells). Figure 3 shows the probability density  
333 function of LANL VTEC – JPL GIM VTEC is plotted for all LANL grid cells (black solid line).  
334 While it is not plotted here, we have looked at the probability density for the new coverage  
335 separately from the cells matched to Madrigal, and the plots are nearly indistinguishable from the  
336 probability density of all LANL cells shown in Figure 3. This indicates that biases and widths are  
337 very similar regardless of whether the JPL GIM cell was well-covered by measurements or not.  
338 The offset between the LANL VTEC and matched JPL GIM data sets is -3 TECU with a FWHM  
339 of 4 TECU. The negative sign on the offset means that JPL GIM generally has a higher TEC  
340 value when compared with LANL VTEC. Given that a constant of 2 TECU is added to the  
341 IONEX data of JPL GIM due to the bias concern when compared with the altimeter TEC data,  
342 the difference between LANL VTEC and JPL GIM would be -1 TECU if that offset were  
343 removed. Figure 4b shows the density plot of all JPL GIM VTEC versus LANL VTEC cells.

344         Given that JPL GIM fills in all cells globally, the comparison of the LANL VTEC data is  
345 a comparison to a global fit rather than specific measurements at certain locations as with the  
346 Madrigal VTEC. Furthermore, while JPL GIM model is driven by global GNSS TEC  
347 measurements, it uses a different set of about 200 IGS receivers than Madrigal GNSS, which

348 uses all available receivers. The similarity between the LANL VTEC comparisons to Madrigal  
349 GNSS and JPL GIM model gives credibility to the LANL VTEC data set.

350 While JPL GIM and Madrigal GNSS VTEC are dependent on ground-based GPS  
351 measurements, and, thus, restricted to land locations, the Jason-3 VTEC measurement is only  
352 made over ocean, so can provide a comparison to LANL VTEC coverage over the oceans.  
353 However, since both LANL VTEC and Jason-3 VTEC are sparse data sets, the number of  
354 matched cells is limited (1594 matching out of 266,630 Jason-3 measurements in 2018). Figure 2  
355 (dashed magenta line) shows the probability density function of the difference between LANL  
356 VTEC and Jason-3 VTEC, with an offset of less than 1 TECU, and a FWHM of about 4 TECU.  
357 Figure 4c shows the 2-D probability density comparison, indicating that these two data sets agree  
358 well for all VTEC values in common.

359 Because the matched number of events between Jason-3 and LANL VTEC are low, we  
360 also plot the probability density of the comparison between Jason-3 and JPL GIM (Figure 3,  
361 dash-dotted red line). The comparison between Jason-3 and JPL GIM is nearly identical to that  
362 between LANL and JPL GIM, giving further evidence that the LANL VTEC data agrees  
363 extremely well with the Jason-3 measurements.

364 Figure 5 shows the number of counts for which each geographical grid cell contained  
365 LANL VTEC data but not Madrigal VTEC data. The red dots show locations of the GNSS  
366 receiver sites used by Madrigal. As expected, LANL VTEC is able to add data in locations with  
367 limited or no GNSS receivers. For the particular time period shown in Figure 1, LANL VTEC is  
368 able to fill in a critical part of the map (central Africa) that was not measured with existing  
369 ground-based GNSS receivers. The IGS receiver placement is also tied to accessible land

370 locations with maintainable internet connects, so we assume that similar regions should be  
371 lacking IGS data as were lacking Madrigal data.

372

## 373 **6 Summary and Discussion**

374 This paper has introduced the LANL VTEC lightning data set, and compared it to the  
375 community data set of Madrigal VTEC from GNSS receivers, the community ionospheric model,  
376 JPL GIM, and oceanic VTEC measurements from Jason-3. Because the sources of error are  
377 independent for these various data sets, the comparisons presented here add confidence to all  
378 datasets. Specifically, these results show the validity of the novel LANL VTEC dataset.

379 We find the LANL data set is offset 3 TECU higher than Madrigal VTEC with a  
380 distribution FWHM of 6 TECU. This finding is consistent with the estimated ionospheric error  
381 of 1-2 TECU from the LANL ray-tracing comparison, and the estimated 2-4 TECU error on  
382 GNSS L-band absolute TEC. Because the comparisons are made between measurements at the  
383 same location and time, this agreement adds confidence to LANL VTEC values globally and  
384 over a wide range of TEC values and ionospheric conditions. This comparison indicates that the  
385 Madrigal VTEC may be leveled (absolute bias) slightly lower than it should be. A further  
386 indication of a lower bias than reality is the finding that Madrigal GNSS VTEC, which includes  
387 plasmaspheric TEC contributions, is found to be lower than Jason-3 VTEC, which does not  
388 include plasmaspheric TEC. More comparisons must be done before fully understanding how  
389 each dataset might need to be adjusted.

390 We find the LANL data set and JPL GIM dataset have an offset of -3 TECU, indicating  
391 that JPL GIM VTEC are typically higher than LANL VTEC by 3 TECU. This includes a bias of

392 +2 TECU on the JPL GIM VTEC based on past comparisons. Thus, the JPL GIM /LANL VTEC  
393 offset may actually be less than 3 TECU. The overall FWHM spread between LANL VTEC and  
394 JPL GIM is 5 TECU. This indicates that JPL GIM may be leveled slightly higher than they  
395 should be, but very comparable with LANL VTEC.

396         While LANL VTEC and Jason-3 VTEC have very limited overlap in their coverage, the  
397 agreement between the two is very good, with an offset of less than 1 TECU. Most grid cells  
398 with overlapping coverage have less than 20 TECU, so this comparison does not address higher  
399 VTEC values. However, the comparison with better statistics between Jason-3 VTEC and JPL  
400 GIM gives similar results to the comparison between LANL VTEC and JPL GIM. This indicates  
401 that it is likely the good agreement between LANL VTEC and Jason-3 VTEC would hold for a  
402 wider range of grid cells.

403         Finally, this paper shows that the LANL VTEC provides additional ionospheric  
404 measurements in regions currently lacking data for global ionospheric models, such as over the  
405 oceans and central Africa. Following papers will delve more deeply into case studies,  
406 particularly looking into geographic differences between LANL VTEC and other data sets.

407

## 408 **Acknowledgments and Data**

409         This work was supported by the DARPA Defense Sciences Office and the Defense  
410 Nuclear Nonproliferation Research and Development Office of the National Nuclear Security  
411 Administration. We gratefully acknowledge the U.S. Dept. of Defense for operating and  
412 providing data from the sensing systems that this work is based on. Research conducted at the Jet

413 Propulsion Laboratory, California Institute of Technology, is under a contract with the National  
414 Aeronautics and Space Administration.

415 The LANL VTEC data are publicly hosted by the National Oceanic and Atmospheric  
416 Administration in NetCDF format and can be found at  
417 <https://www.ncei.noaa.gov/archive/accession/0241206>. MIT Haystack Madrigal VTEC data can  
418 be found at <http://www.openmadrigal.org>. JPL IONEX data can be found at  
419 [https://cdis.nasa.gov/Data\\_and\\_Derived\\_Products/GNSS/atmospheric\\_products.html#iono](https://cdis.nasa.gov/Data_and_Derived_Products/GNSS/atmospheric_products.html#iono).  
420 Jason-3 data are available at <https://www.ncei.noaa.gov/data/oceans/jason3/gdr/gdr/>.

421 GPS TEC data products and access through the Madrigal distributed data system are  
422 provided to the community (<http://cedar.openmadrigal.org>) by the Massachusetts Institute of  
423 Technology (MIT) under support from US National Science Foundation grant AGS-1952737.  
424 Data for TEC processing is provided from the following organizations: UNAVCO, Scripps Orbit  
425 and Permanent Array Center, Institut Geographique National, France, International GNSS  
426 Service, The Crustal Dynamics Data Information System (CDDIS), National Geodetic Survey,  
427 Instituto Brasileiro de Geografia e Estatística, RAMSAC CORS of Instituto Geográfico Nacional  
428 de la República Argentina, Arecibo Observatory, Low-Latitude Ionospheric Sensor Network  
429 (LISN), Topcon Positioning Systems, Inc., Canadian High Arctic Ionospheric Network, Centro  
430 di Ricerche Sismologiche, Système d'Observation du Niveau des Eaux Littorales (SONEL),  
431 RENAG : REseau NATIONAL GPS permanent, GeoNet - the official source of geological hazard  
432 information for New Zealand, GNSS Reference Networks, Finnish Meteorological Institute, and  
433 SWEPOS - Sweden.

434

435 **References**

436 Abarca, S. F., Corbosiero, K. L., & Galarneau, T. J. Jr. (2010). An evaluation of the Worldwide  
437 Lightning Location Network (WWLLN) using the National Lightning Detection Network  
438 (NLDN) as ground truth. *J. of Geophys. Res.*, *15*, D18206, doi:10.1029/2009JD013411.

439 Azeem, I., Yue, J., Hoffmann, L., Miller, S. D., Straka, W. C. III, & Crowley, G. (2015).  
440 Multisensor profiling of a concentric gravity wave event propagating from the troposphere  
441 to the ionosphere. *Geophysical Research Letters*, *42*, 7874–7880,  
442 doi:10.1002/2015GL065903.

443 Bilitza, D., L.-A. McKinnell, B. Reinisch, and T. Fuller-Rowell (2011), The international  
444 reference ionosphere today and in the future, *J. Geod.*, *85*:909-920, doi:10.1007/s00190-  
445 010-0427-x.

446 Born, M. and E. Wolf (1999), *Principles of Optics*. Cambridge University Press, 7th ed.

447 Burrell, A. G., N. A. Bonito, and C. S. Carrano (2009), Total electron content processing from  
448 GPS observations to facilitate ionospheric modeling, *GPS Solutions*, *13*(2),  
449 doi:10.1007/s10291-008-0102-3.

450 Coster, A. and S. Skone (2009), Monitoring storm-enhanced density using IGS reference station  
451 data, *J. Geod.*, *83*:345–351, doi:10.1007/s00190-008-0272-3.

452 Decker, D. T., and L. F. McNamara (2007), Validation of ionospheric weather predicted by  
453 Global Assimilation of Ionospheric Measurements (GAIM) models, *Radio Sci.*, *42*, RS4017,  
454 doi:10.1029/2007RS003632.

- 455 Deng, A., & Stauffer, D. R. (2006), On improving 4-km mesoscale model simulations. *Journal*  
456 *of Applied Meteorology and Climatology*, 45(3), 361–381, doi:10.1175/JAM2341.1.
- 457 Dowden, R. L., Brundell, J. B., & Rodger, C. J. (May 2002). VLF lightning location by time of  
458 group arrival (TOGA) at multiple sites. *J.of Atmos. and Solar-Terr. Phys.*, 64(7), 817–830,  
459 doi:10.1016/S1364-6826(02)00085-8.
- 460 Dumont, J., Rosmorduc, V., Carrere, L., Picot, N., Bronner, E., Couhert, A., Guillot, A., Desai,  
461 S., Benekamp, H., 2017b. Jason-3 Products Handbook, CNES: SALP-MU-M-OP-16118-  
462 CN, Issue 1 rev 4, January 16th 2017.
- 463 Iijima, B.A., I.L. Harris, C.M. Ho, U.J. Lindqwister, A.J. Mannucci, X. Pi, M.J. Reyes, L.C.  
464 Sparks, B.D. Wilson (1999), Automated daily process for global ionospheric total electron  
465 content maps and satellite ocean altimeter ionospheric calibration based on Global  
466 Positioning System data, *J. Atmos. and Solar-Terr. Phys.* 61, pp.1205-1218,  
467 doi:10.1016/S1364-6826(99)00067-X.
- 468 Imel, D.A., 1994. Evaluation of the TOPEX/POSEIDON dual-frequency ionosphere correction.  
469 *J. Geophys. Res.* 99 (C12), doi:10.1029/94JC01869.
- 470 Jakowski, N., C. Mayer, M. M. Hoque, and V. Wilken (2011), Total electron content models and  
471 their use in ionosphere monitoring, *Radio Sci.*, 46, RS0D18, doi:10.1029/2010RS004620.
- 472 Kelley, M. C. (2009). *The Earth's ionosphere*. London: Academic.
- 473 Lay, E. H. (2018). Ionospheric irregularities and acoustic/gravity wave activity above low-  
474 latitude thunderstorms. *Geophys. Res. Lett.*, 45, doi:10.1002/2017GL076058.

- 475 Lay, E. H., P.A. Parker, M.E. Light, and P. Colestock (2018), Estimate of errors induced by first  
476 order Appleton-Hartree approximation, Los Alamos National Laboratory, LA-UR-18-  
477 20440.
- 478 Lay, E. H., X.-M. Shao, A. K. Kendrick, and C. S. Carrano (2015), Ionospheric acoustic and  
479 gravity waves associated with midlatitude thunderstorms, *J. Geophys. Res. Space Physics*,  
480 *120*, doi:10.1002/2015JA021334.
- 481 Lay, E. H., S. Close, P. Colestock, and G. Bust (2011), Development and error analysis of  
482 nonlinear ionospheric removal algorithm for ionospheric electron density determination  
483 using broadband RF data, *J. Geophys. Res.*, *116*, A02316, doi:10.1029/2010JA015862.
- 484 Lay, E. H., Holzworth, R. H., Thomas, J. N., Dowden, R. L., Rodger, C. J., & Pinto Jr., O.  
485 (2004). WWLL global lightning detection system: Regional validation study in Brazil.  
486 *Geophys. Res. Lett.*, *31*, L03102, doi:10.1029/2003GL018882.
- 487 Mandrake, L., B. Wilson, C. Wang, G. Hajj, A. Mannucci, and X. Pi (2005), A performance  
488 evaluation of the operational Jet Propulsion Laboratory/University of Southern California  
489 Global Assimilation Ionospheric Model (JPL/USC GAIM), *J. Geophys. Res.*, *110*, A12306,  
490 doi:10.1029/2005JA011170.
- 491 Mannucci, A. J., B. D. Wilson, D. N. Yuan, C. H. Ho, U. J. Lindqwister, and T. F. Runge (1998),  
492 A global mapping technique for GPS-derived ionospheric total electron content  
493 measurements, *Radio Sci.*, *33*(3), pp.565-582, doi:10.1029/97RS02707.
- 494 Mannucci, A. J., B. T. Tsurutani, B. A. Iijima, A. Komjathy, A. Saito, W. D. Gonzalez, F. L.  
495 Guarnieri, J. U. Kozyra, and R. Skoug (2005), Dayside global ionospheric response to the

- 496 major interplanetary events of October 29–30, 2003 “Halloween Storms”, *Geophys. Res.*  
497 *Lett.*, *32*, L12S02, doi:10.1029/2004GL021467.
- 498 Moses, R. W., and A. R. Jacobson (2004), Ionospheric profiling through radio-frequency signals  
499 recorded by the FORTE satellite, with comparison to the International Reference  
500 Ionosphere, *Adv. Space Res.*, *34*, 2096–2103, doi:10.1016/j.asr.2004.02.018.
- 501 Nava, B., Coisson, P., & Radicella, S. M. (2008). A new version of the NeQuick ionosphere  
502 electron density model. *J. of Atmos. and Sol.-Terr. Phys.*, *70*(15), 1856–1862,  
503 doi:10.1016/j.jastp.2008.01.015.
- 504 Rideout, W. and A. Coster, (2006), Automated GPS processing for global total electron content  
505 data, *GPS Solutions*, doi:10.1007/s10291-006-0029-5.
- 506 Roussel-Dupre, R.A., Jacobson, A.R., Triplett, L.A (2001). Analysis of FORTE data to extract  
507 ionospheric parameters, *Radio Sci.* *36* (6), 1615–1630, doi:10.1029/2000RS002587.
- 508 Sardón, E., and N. Zarraoa (1997), Estimation of total electron content using GPS data: How  
509 stable are the differential satellite and receiver instrumental biases?, *Radio Sci.*, *32*, 1899-  
510 1910, doi:10.1029/97RS01457.
- 511 Scherliess, L., D.C. Thompson and R.W. Schunk (2009), Ionospheric dynamics and drivers  
512 obtained from a physics-based data assimilation model, *Radio Sci.*, *44*, RS0A32, doi:  
513 10.1029/2008RS004068.
- 514 Scherliess, L., R.W. Schunk, J.J. Sojka, D.C. Thompson and L. Zhu (2006), Utah State  
515 University Global Assimilation of Ionospheric Measurements Gauss-Markov Kalman filter

- 516 model of the ionosphere: Model description and validation, *J. Geophys. Res.*, *111*, A11315,  
517 doi: 10.1029/2006JA011712.
- 518 Schunk, R. W., et al. (2004), Global Assimilation of Ionospheric Measurements (GAIM), *Radio*  
519 *Sci.*, *39*, RS1S02, doi:10.1029/2002RS002794.
- 520 Schunk, R. W., and J. J. Sojka (1996), Ionosphere-thermosphere space weather issues, *J. Atmos.*  
521 *Sol. Terr. Phys.*, *58*, 1527–1574, doi: 10.1016/0021-9169(96)00029-3.
- 522 Vierinen, J., Coster, A. J., Rideout, W. C., Erickson, P. J., and Norberg, J.: Statistical framework  
523 for estimating GNSS bias, *Atmos. Meas. Tech.*, *9*, 1303-1312, 10.5194/amt-9-1303-2016,  
524 2016.
- 525 Wang, W., J. Lei, A. G. Burns, S. C. Solomon, M. Wiltberger, J. Xu, Y. Zhang, L. Paxton, and  
526 A. Coster (2010), Ionospheric response to the initial phase of geomagnetic storms: Common  
527 features, *J. Geophys. Res.*, *115*, A07321, doi:10.1029/2009JA014461.
- 528 Yasyukevich, Yu.V., E.L. Afraimovich, K.S. Palamartchouk, P.V. Tatarinov (2010), Cross  
529 testing of ionosphere models IRI-2001 and IRI-2007, data from satellite altimeters  
530 (Topex/Poseidon and Jason-1) and global ionosphere maps, *Advances in Space Research*,  
531 *46*(8), doi:10.1016/j.asr.2010.06.010.
- 532 Yizengaw, E., M. B. Moldwin, A. Komjathy, and A. J. Mannucci (2006), Unusual topside  
533 ionospheric density response to the November 2003 superstorm, *J. Geophys. Res.*, *111*,  
534 A02308, doi:10.1029/2005JA011433.
- 535

536 **Figure Captions**

537

538 **Figure 1.** 1-hour snapshot at 18:30:00UT 09 June 2018 of gridded global VTEC for JPL GIM  
539 (top) Madrigal GNSS (middle) and LANL VTEC (bottom).

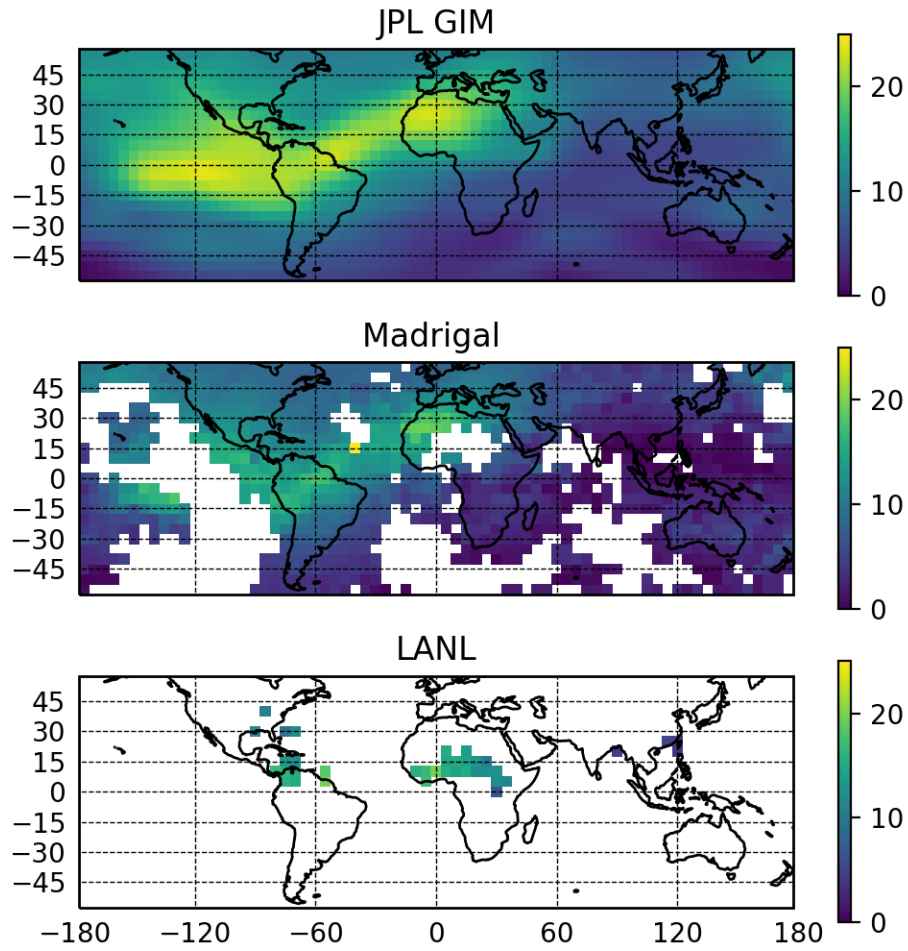
540 **Figure 2.** A 2-D probability density plot of TEC difference introduced by ionospheric variability  
541 and geometry between the known VTEC (x-axis) and the estimated LANL VTEC (y-axis).

542 **Figure 3.** A probability density plot generated from the difference between LANL VTEC and:  
543 Madrigal VTEC for matched cells (blue thin solid), JPL GIM (black thick solid), Jason-3  
544 (magenta dashed). Red dash-dotted line shows Jason-3 – JPL GIM VTEC.

545 **Figure 4.** 2-D probability density plots of (a) Madrigal VTEC, (b) JPL-GIM VTEC, and (c)  
546 Jason-3 VTEC on x-axis and LANL VTEC on y-axis. Colorbar represents density in counts per  
547 sq. TECU unit area / total counts.

548 **Figure 5.** Counts of grid cells with LANL VTEC without comparable Madrigal VTEC gridded  
549 data. The most notabled areas of increased coverage are in continental Africa, southwest of  
550 Mexico, and over the oceans. The first two areas correlate well to significant lightning activity.

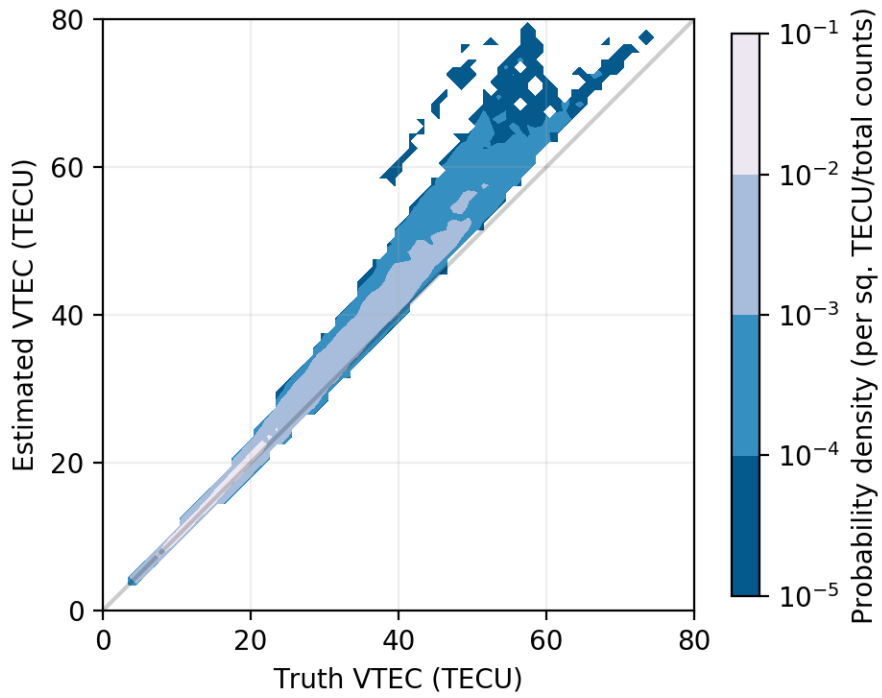
551

552 **Figures**

553

554 **Figure 1.** 1-hour snapshot at 18:30:00UT 09 June 2018 of gridded global VTEC for IONEX

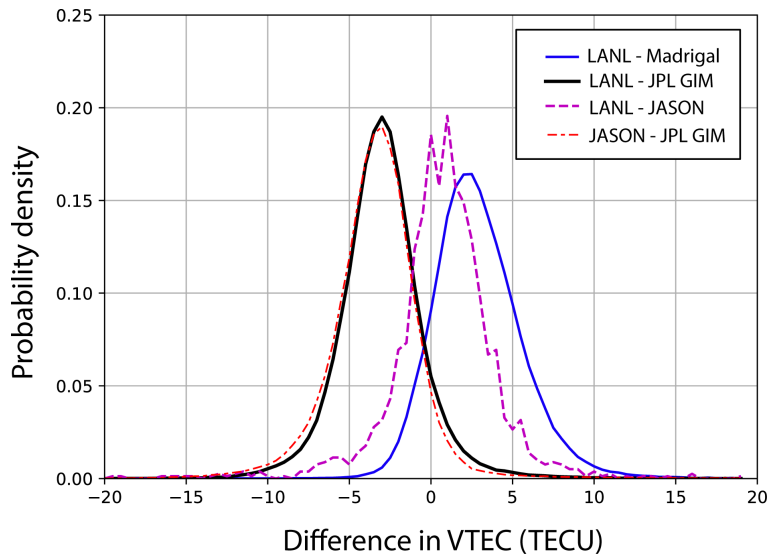
555 TEC data of JPL GIM (top) Madrigal GNSS (middle) and LANL VTEC (bottom).



556

557 **Figure 2.** A 2-D probability density plot of TEC difference introduced by ionospheric variability  
558 and geometry between the known VTEC (x-axis) and the estimated LANL VTEC (y-axis).

559

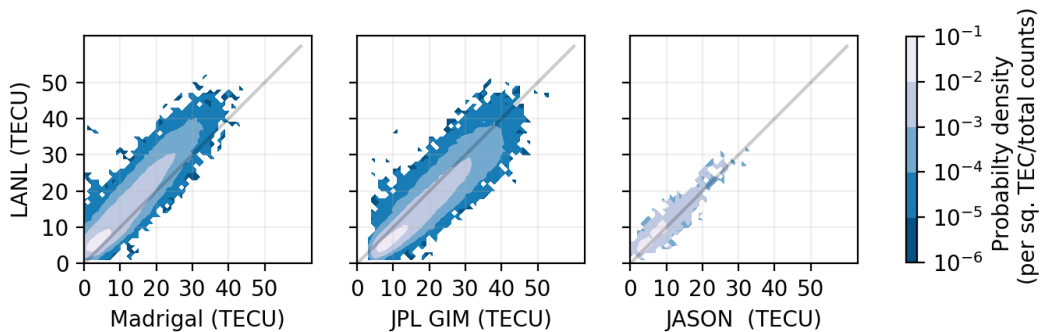


560

561 **Figure 3.** A probability density function generated from the difference between LANL VTEC  
 562 and: Madrigal VTEC for matched cells (blue thin solid), JPL GIM (black thick solid), Jason-3  
 563 (magenta dashed). Red dash-dotted line shows Jason-3 – JPL GIM IONEX VTEC.

564

565

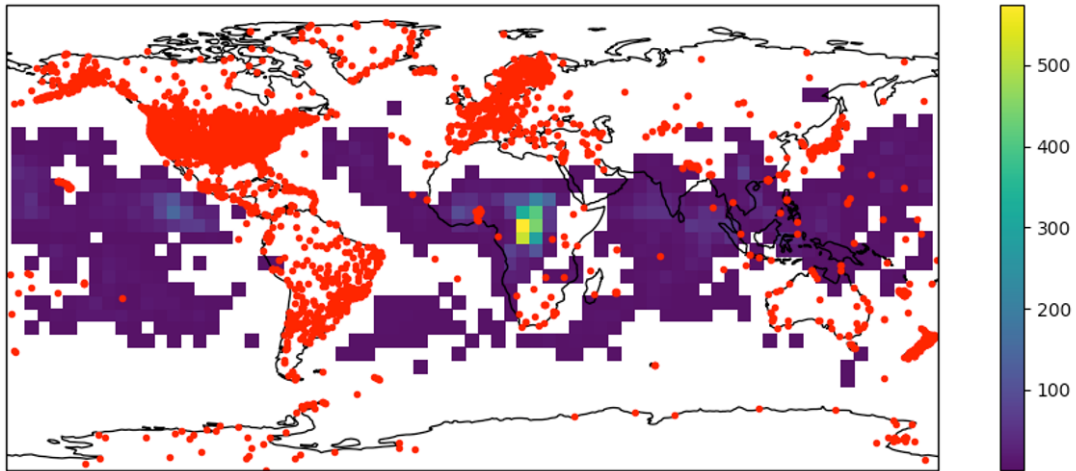


566

567 **Figure 4.** 2-D probability density plots of (a) Madrigal VTEC, (b) JPL-GIM IONEX VTEC, and  
 568 (c) Jason-3 VTEC on x-axis and LANL VTEC on y-axis. Colorbar represents density in counts  
 569 per sq. TECU unit area / total counts.

570

Counts of grid cell when LANL VTEC data contains data without corresponding GNSS TEC data



571

572 **Figure 5.** Counts of grid cells with LANL VTEC without comparable Madrigal VTEC gridded  
573 data. The most notable areas of increased coverage are in continental Africa, southwest of  
574 Mexico, and over the oceans. The first two areas correlate well to significant lightning activity.